Flow around topological defects in active nematic films

Jonas Rønning[1], Cristina M. Marchetti[2],
Mark J. Bowick[3] and Luiza Angheluta[1]

[1]Njord Centre, Department of Physics, University of Oslo, PO Box 1048, Oslo 0316, Norway
[2]Department of Physics, University of California Santa Barbara, Santa Barbara, CA 93106, USA
[3]Kavli Institute for Theoretical Physics, University of California Santa Barbara, Santa Barbara, CA 93106, USA

JR, 0000-0001-5289-7276

We study the active flow around isolated defects and the self-propulsion velocity of $+1/2$ defects in an active nematic film with both viscous dissipation (with viscosity η) and frictional damping Γ with a substrate. The interplay between these two dissipation mechanisms is controlled by the hydrodynamic dissipation length $\ell_d = \sqrt{\eta/\Gamma}$ that screens the flows. For an isolated defect, in the absence of screening from other defects, the size of the shear vorticity around the defect is controlled by the system size R. In the presence of friction that leads to a finite value of ℓ_d, the vorticity field decays to zero on the lengthscales larger than ℓ_d. We show that the self-propulsion velocity of $+1/2$ defects grows with R in small systems where $R < \ell_d$, while in the infinite system limit or when $R \gg \ell_d$, it approaches a constant value determined by ℓ_d.

1. Introduction

Active matter consists of collections of individuals that dissipate energy taken from the environment to generate motion and forces and self-organize into a rich variety of ordered phases. Many active systems exhibit nematic order interrupted by orientational defects and advected by spontaneous flows driven by intrinsic activity of the self-propelled individuals. This behaviour is found in reconstituted systems, such as mixtures of cytoskeletal filaments and motor proteins [1–4], bacterial suspensions [5,6] and cell sheets [7,8], as well as synthetic systems, like vertically vibrated layers of granular rods [6,9].
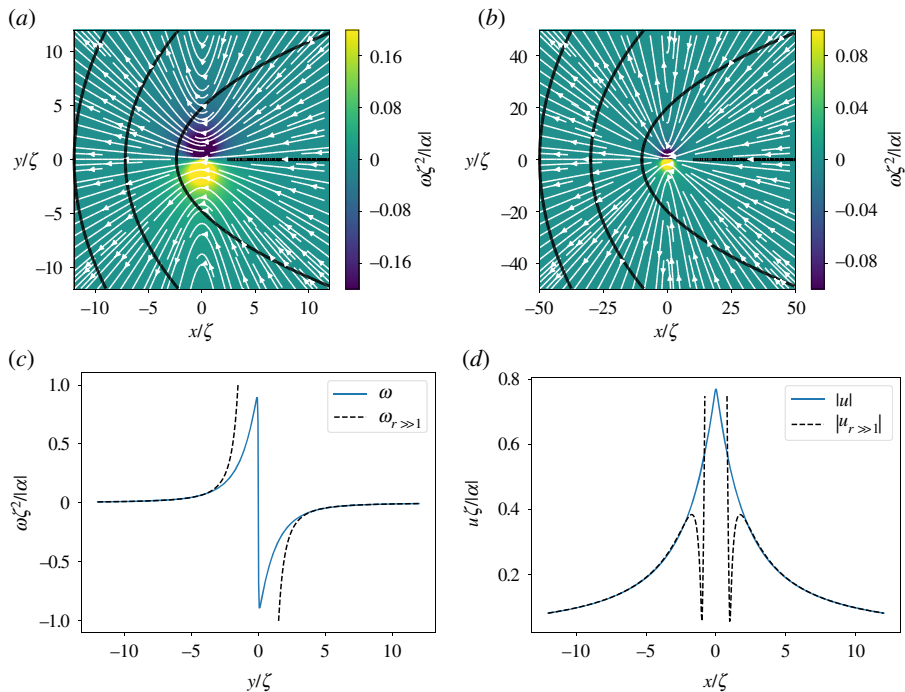
Figure 1. Flow streamlines (white arrow) around a $+1/2$ defect for $\alpha < 0$ obtained from (*a*) full solution and (*b*) asymptotic one. The nematic director field is shown in black lines and the background colour map denotes vorticity. To show the structure of the near-field, the vorticity scale is saturated at ± 0.2 in (*a*) and at ± 0.1 in (*b*). (*c*) Cross section of vorticity obtained from the exact solution (solid blue line) and the asymptotic limit (dotted black line) at $x = 0$ as a function of y. (*d*) Cross section of the velocity obtained from the exact solution (solid blue line) and the asymptotic limit (dotted black line) at $y = 0$ as a function of x. (Online version in colour.)

A central feature of active nematics is the feedback between active stresses, which distort orientational order and the spontaneous flow generated by such distortions. In hydrodynamic descriptions [6], the active stress σ_{ij}^{a} exerted by elongated active entities on the surrounding fluid is proportional to the nematic order parameter tensor Q_{ij}, namely $\sigma_{ij}^{a} = \alpha_0 Q_{ij}$ [10,11]. The activity coefficient α_0 embodies the microscale biomolecular processes that convert chemical energy into mechanical forces, and depends on the concentration of active entities, which in general may vary in space and time [12,13]. The sign of α_0 distinguishes between contractile ($\alpha_0 > 0$) stress generated by 'puller' swimmers, such as the algae Chlamydomonas, versus extensile ($\alpha_0 < 0$) stress generated by 'pusher' swimmers, e.g. most flagellated bacteria. Its magnitude controls the strength of the active flow. Fluctuations in orientational order yield active stresses and associated flows, which can in turn enhance the orientational distortions. The resulting feedback loop destabilizes the nematic order, driving the system to a state of self-sustained spatio-temporally chaotic flow, with proliferation of topological defects, and termed active turbulence [14,15].

The lowest-energy orientational defects in nematic films have half-integer topological charge and opposite sign. The $+1/2$ defects have a comet-like shape, while the $-1/2$ defects have a tri-fold symmetry (figures 1 and 2). Defects strongly disrupt orientational order and induce long-range nematic distortions. In active systems, such distortions generate flows with symmetry and profiles controlled by the defect geometry. The nematic distortion created by a $+1/2$ defect yields an active flow that is finite at the defect core. A $+1/2$ defect then rides along with the flow it itself generates, behaving like a motile particle with a non-vanishing self-propulsion velocity $\mathbf{v}_{+}^{a}$, even in the absence of external drive [12,16]. On the other hand, the active backflow generated by a $-1/2$ defect vanishes at the core due to the defect's threefold symmetry (figure 2). Thus
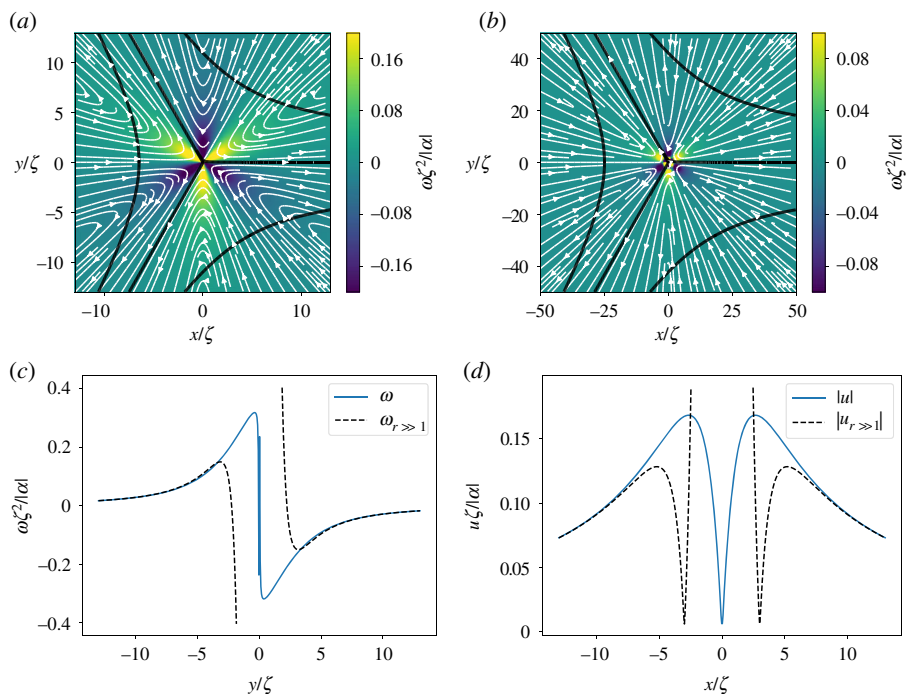
Figure 2. Flow streamlines (white arrow) around a $-1/2$ defect for $\alpha < 0$ obtained from (a) full solution and (b) asymptotic one. The nematic director field is shown in black lines and the background colour map denotes vorticity. To show the structure of the near-field, the vorticity scale is saturated at ± 0.2 in (a) and at ± 0.1 in (b). (c) Cross section of vorticity obtained from the exact solution (solid blue line) and the asymptotic limit (dotted black line) at $x = 0$ as a function of y. Note that the vortices changes sign rapidly at origin due to its multi-valued phase (see equation (4.6)). (d) Cross section of the velocity obtained from the exact solution (solid blue line) and the asymptotic limit (dotted black line) at $y = 0$ as a function of x. (Online version in colour.)

$-1/2$ defects behave like passive particles and have no spontaneous motility in the absence of external driving. A simple estimate demonstrates that $\mathbf{v}_+^a$ is directed along the polar axis of the $+1/2$ defect and is proportional to the activity α_0. In an extensile medium $+1/2$ defects self-propel in the direction of the head of the comet, while in a contractile system they move towards the comet's tail [12,16,17]. The direction of motion of $+1/2$ defects can then be used as a metric for determining the nature of active stress in the system. Such measurements have, for instance, revealed the surprising dominance of extensile stresses in confluent tissue composed of tightly bound contractile individual cells [18–22].

The flow generated by defects and the resulting propulsive speed of the $+1/2$ also vary depending on the dissipative processes at play in the system and the role of fluid incompressibility. Specifically, important differences exist between 'dry' systems, where dissipation is dominated by friction Γ with a substrate or an external medium [23,24] and 'wet' systems, where dissipation is mainly controlled by viscosity η, resulting in long-range hydrodynamic effects [14,17,24,25]. In incompressible wet systems, activity is also a source of pressure gradients, which in turn contribute alongside with the nematic distortion to the self-motility of positive defects. In the limit of viscous dominated flows with no friction with the substrate, the self-propulsion speed scales as $|\mathbf{v}_+^a| \sim (|\alpha_0|/\eta)\ell$, where ℓ is a length scale given by the system size for an isolated defect [17] or by the mean separation between defects, which is, in turn, controlled by the active length scale $\ell_a = \sqrt{K/|\alpha_0|}$, with K the nematic stiffness [17]. In overdamped (dry) systems, where viscosity is negligible compared with frictional damping with the substrate, $|\mathbf{v}_+^a| \sim |\alpha_0|/(\xi\Gamma)$, where ξ is the nematic coherence length [23,24,26]. A complete
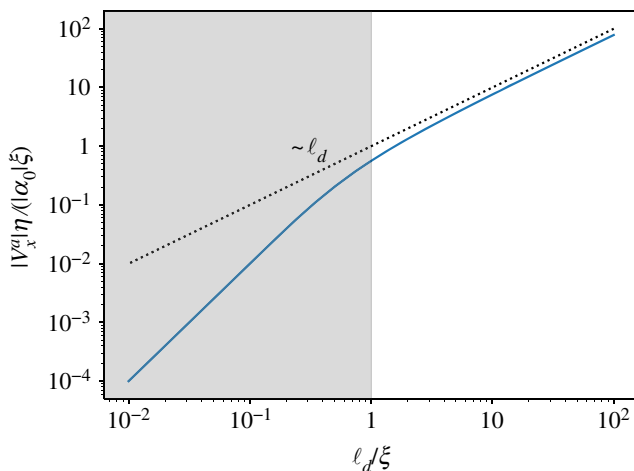
Figure 3. The self-propulsion speed of a $+1/2$ defect as function of ℓ_d/ξ in an unbounded system. The line is the exact analytical solution, while the dotted line shows the asymptotic scaling with ℓ_d, i.e. $v_x^a \eta \sim \ell_d$ for $\ell_d > \xi$. The grey area corresponds to the overdamped limit, where essentially v_x^a depends solely on friction. (Online version in colour.)

calculation of the active flows associated with defect configurations and of the propulsive speed of the $+1/2$ defect that bridges between the two limits is, however, not available. The need for such a calculation is further motivated by recent work that has shown that tuning frictional damping relative to viscous dissipation leads to different dynamical regimes and ordering behaviour of interacting defects [27].

In this paper, we present a detailed calculation of the flow around isolated $\pm 1/2$ defects and of the defect's self-propulsion velocity in an incompressible nematic film. We incorporate both viscous dissipation and frictional damping and examine the interplay between the two, as well as the long-range hydrodynamic effects arising from incompressibility. We evaluate the $+1/2$ self-propulsive speed $|\mathbf{v}_+^a|$ as a function of the hydrodynamic dissipation length $\ell_d = \sqrt{\eta/\Gamma}$, which measures the competition between viscous dissipation and frictional damping. The result is summarized in figure 3. When dissipation is controlled by friction ($\ell_d \ll \xi$), one recovers the simple dimensional estimate $|\mathbf{v}_+^a| \sim |\alpha_0|/(\xi \Gamma)$. We show, however, that to obtain this result it is not sufficient to consider the far flow field which diverges near the defect, but one must resolve the full flow field near the defect core. On the other hand, when viscous stresses dominate, the defect propulsive speed depends on the order of limits. If $\Gamma = 0$ from the outset, then a simple estimate yields $v_x^a \sim r$ due to the long-range nature of defect distortions. This limit, however, corresponds to a 'floating' layer and does not describe experimental situations where the active nematic film is supported by a substrate [25] or in contact with other fluids. It has been argued before that this unbounded growth should be cut off either by the system size or by the defect separation [17]. Our work shows that a finite friction cuts off the large-scale divergence of the defect self-propulsion speed at the scale ℓ_d, with $|\mathbf{v}_+^a| \sim (|\alpha_0|/\eta)\ell_d$ in the limit $\zeta = \ell_d/\xi \gg 1$, where viscous dissipation exceeds frictional drag and provides an analytical expression for the defect self-propulsion over all values of friction and viscosity. We find that the structure of the flow field around a defect is also affected by the competition between viscosity and friction. At distances large compared with ℓ_d, the flow velocity decays in the far-field as $\sim 1/r$, due to friction with the substrate [25]. At distances smaller than ℓ_d, viscous dissipation dominates and smooths out the velocity field near the defect core. Our work is relevant to defects in thin film of microtubule nematics on a substrates, as well as to dense cell layers.

In §2, we describe the hydrodynamic model. In §§3 and 4, we provide analytical derivations of closed expressions for the velocity and pressure fields induced by $\pm 1/2$ defects in an infinite

system. One implication of the long-range interactions present in active nematics is that there are strong finite-size effects on the single defect flow field. This is discussed in §5, where we compare the analytical predictions with numerical integration of the Stokes equations in a disc of finite radius. Finally, the main results are discussed with concluding remarks in §6.

2. Hydrodynamic model

We consider a hydrodynamic model of an active nematic that couples flow velocity $\mathbf{u}(\mathbf{r})$ to the nematic order parameter $Q_{ij} = S(\hat{n}_i \hat{n}_j - \frac{1}{2}\delta_{ij})$, where S quantifies the degree of order and $\hat{\mathbf{n}}(\mathbf{r}) = (\cos\theta(\mathbf{r}), \sin\theta(\mathbf{r}))$ is the orientational director field with head-tail symmetry. In the simplest formulation, we consider that the $\mathbf{Q}$-tensor is a minimizer of the de Gennes–Landau free energy [6]

$$\mathcal{F} = \int d\mathbf{r} \left[\frac{K}{2}|\nabla Q|^2 + \frac{g}{4}\left(1 - \frac{1}{2}\mathrm{Tr}(Q^2)\right)^2 \right], \tag{2.1}$$

with isotropic elastic constant $K > 0$ and g the strength of the local ordering potential. The uniform nematic ordered state corresponds to $S_0^2 = 1$. The flow field satisfies a Stokes equation that balances forces on a fluid element, given by [6]

$$(\Gamma - \eta\nabla^2)\mathbf{u} = \alpha_0 \nabla \cdot Q(\mathbf{r}) - \nabla p(\mathbf{r}), \quad \nabla \cdot \mathbf{u} = 0, \tag{2.2}$$

where Γ is a friction coefficient per unit area, η is the dynamic viscosity and α_0 is the activity parameter, with dimensions of stress. For simplicity, we neglect the elastic stress as being of higher order in the gradients of $\mathbf{Q}$ compared with the active stress and a more important contribution for nematic textures with many defects. Here, we consider the flow field generated by an isolated $\pm 1/2$ defect embedded in an otherwise uniform nematic field.

In two dimensions, the traceless $\mathbf{Q}$-tensor has two independent components and can be represented equivalently as a complex scalar order parameter $\psi = Q_{xx} + iQ_{xy}$. The configuration of a defect located at the origin can be written in terms of the ψ-field as $\psi(\mathbf{r}) = S(r)e^{2i\theta(\mathbf{r})}$, where $r \equiv |\mathbf{r}|$. The detailed form of core function $S(r)$ depends on the specific terms retained in the free energy, but it has the important generic asymptotic behaviours that $S(r) \to 1$ for $r \gg \xi$ and $S(r) \approx ar/\xi$ when $r \to 0$, where $\xi = \sqrt{K/g}$ is the coherence length that sets the scale of the defect core and a is a numerical constant $\mathcal{O}(1)$. Below we set $a = 1$, without loss of generality. The coherence length provides an ultraviolet cutoff to separate inner core-solution from outer-core solution. On long distances, the nematic orientation is a potential field that has a branch cut starting at the origin where there is an isolated defect of charge $q = \pm 1/2$ and can be written as [24,28]

$$\theta(\mathbf{r}) = q\arctan\left(\frac{y}{x}\right) + \theta_0, \tag{2.3}$$

where θ_0 is the uniform background orientation. Without loss of generality, we set $\theta_0 = 0$.

We rescale the Stokes equation in units of the nematic relaxation time $\tau = \gamma/g$ (where γ is the inverse of the rotational diffusivity) and the coherent length ξ, such that the dimensionless momentum equation takes the form

$$(1 - \zeta^2\nabla^2)\mathbf{u} = \mathbf{F}^{\pm} - \nabla\tilde{p}(\mathbf{r}), \quad \nabla \cdot \mathbf{u} = 0, \tag{2.4}$$

where $\mathbf{F}^{\pm} = \alpha\nabla \cdot Q$ is the active force generated by a defect. The rescaled activity and pressure are given by $\alpha = \alpha_0\gamma/(\Gamma K)$ and $\tilde{p} = p\gamma/(\Gamma K)$. The dimensionless parameter $\zeta = \sqrt{\eta/(\Gamma\xi^2)} = \ell_d/\xi$ measures the hydrodynamic dissipation length $\ell_d = \sqrt{\eta/\Gamma}$ in units of the coherent length, ξ. In the following, we will omit the tilde and all quantities are dimensionless unless otherwise stated.

The components of the **Q** tensor for an isolated $+1/2$ defect are given by $Q_{xx}(\mathbf{r}) = S(r)(x/r)$ and $Q_{xy} = S(r)(y/r)$. The active force density then reduces to

$$\mathbf{F}^+(\mathbf{r}) = \begin{cases} 2\alpha\mathbf{e}_x, & r \to 0, \\ \frac{\alpha}{r}\mathbf{e}_x, & r \gg 1. \end{cases} \tag{2.5}$$

Similarly, for a negative defect $Q_{xx} = S(r)(x/r)$ and $Q_{xy} = -S(r)(y/r)$, corresponding to an active force density given by

$$\mathbf{F}^-(\mathbf{e}) = \begin{cases} 0, & r \to 0 \\ -\alpha\frac{x^2-y^2}{r^3}\mathbf{e}_x + \alpha\frac{2xy}{r^3}\mathbf{e}_y, & r \gg 1. \end{cases} \tag{2.6}$$

The solutions for the flow velocity and pressure can be written in terms of the corresponding Green functions as

$$\mathbf{u}(\mathbf{r}) = \frac{1}{2\pi\zeta^2}\int d\mathbf{r}' K_0(\frac{|\mathbf{r} - \mathbf{r}'|}{\zeta})[\mathbf{F}^\pm(\mathbf{r}') - \nabla'p(\mathbf{r}')] \equiv \mathbf{u}^a + \mathbf{u}^p \tag{2.7}$$

and

$$p(\mathbf{r}) = \frac{1}{2\pi}\int d\mathbf{r}' \ln(|\mathbf{r} - \mathbf{r}'|)\nabla' \cdot \mathbf{F}^\pm(\mathbf{r}'), \tag{2.8}$$

where $\mathbf{u}^a$ and $\mathbf{u}^p$ are the contributions to the flow velocity induced by the active stress and pressure gradients, respectively. Note that the latter also depends (indirectly) on activity. In the limit of no friction, equations (2.7) and (2.8) reduce to equations (3.7) and (3.8) of [17].

3. Positive nematic defect in an infinite system

(a) Defect self-propulsion

The net active flow at the defect core acts as an advective velocity that propels the defect with a velocity $\mathbf{v}^a$, which in turn is controlled by both the active stress and pressure gradients. Thus we write $\mathbf{v}^a = \mathbf{u}^a(0) + \mathbf{u}^p(0)$. The flow induced by the active stress at the origin is given by equation (2.7) evaluated at $\mathbf{r} = 0$. The y-component vanishes due to symmetry considerations, and the x-component is given by

$$u_x^a(0) = 2\alpha\left[1 - \frac{1}{\zeta}K_1(\zeta^{-1})\right] + \frac{\pi\alpha}{2\zeta}\left[1 - \frac{1}{\zeta}(L_{-1}(\zeta^{-1})K_0(\zeta^{-1}) + L_0(\zeta^{-1})K_1(\zeta^{-1}))\right], \tag{3.1}$$

where $\zeta = \ell_d/\xi$, $K_n(x)$ are modified Bessel functions and $L_n(x)$ modified Struve function.

The integral determining the pressure field given by equation (2.8) can be performed by a mapping to complex coordinates $(x',y') \to (w,\bar{w})$, $(x,y) \to (z,\bar{z})$ and then using the substitution to polar coordinates $w = r'\hat{w}$, $\hat{w} = e^{i\theta'}$. This yields

$$p(\mathbf{r}) = -\frac{\alpha}{2i\pi}\int_0^1 dr'r' \oint_\gamma d\hat{w}\left(\frac{1}{\hat{w}r'(\hat{w} - zr'^{-1})} - \frac{1}{\bar{z}(\hat{w} - r'\bar{z}^{-1})}\right)$$
$$- \frac{\alpha}{4i\pi}\int_1^\infty dr' \oint_\gamma d\hat{w}\left(\frac{1}{\hat{w}r'(\hat{w} - zr'^{-1})} - \frac{1}{\bar{z}(\hat{w} - r'\bar{z}^{-1})}\right) \tag{3.2}$$

with γ a contour of unit radius centred at origin. The pole at $\hat{w} = 0$ is always inside the unit disc $|\hat{w}| < 1$, whereas the poles at $\hat{w} = zr'^{-1}$ and $\hat{w} = r'\bar{z}^{-1}$ are inside the unit disc when $|z| < r'$ or $|z| > r'$, respectively. The contour integrals are then evaluated using the residue theorem. Integrating over

r', we finally obtain

$$p(\mathbf{r}) = \begin{cases} \alpha x, & r < 1, \\ \frac{\alpha x}{r}, & \text{if } r > 1. \end{cases} \tag{3.3}$$

Consequently, the defect self-propulsion induced by pressure gradient has only an x-component, which counteracts that induced by the active stress, and given by

$$u_x^p(0) = -\alpha \left(1 - \frac{1}{\zeta} K_1(\zeta^{-1}) \right) - \frac{\pi \alpha}{4\zeta} \left[1 - \frac{1}{\zeta} [L_{-1}(\zeta^{-1}) K_0(\zeta^{-1}) + L_0(\zeta^{-1}) K_1(\zeta^{-1})] \right]$$

$$= -\frac{u_x^a(0)}{2}. \tag{3.4}$$

Combining these results, we find that the self-propulsion velocity of an isolated $+1/2$ defect oriented along the x-axis is $\mathbf{v}^a = v_x^a \hat{\mathbf{e}}$, where v_x^a has the following scaling form:

$$v_x^a = \alpha F(\zeta), \tag{3.5}$$

where

$$F(\zeta) = \left(1 - \frac{1}{\zeta} K_1(\zeta^{-1}) \right) + \frac{\alpha \pi}{4\zeta} \left[1 - \frac{1}{\zeta} [L_{-1}(\zeta^{-1}) K_0(\zeta^{-1}) + L_0(\zeta^{-1}) K_1(\zeta^{-1})] \right]. \tag{3.6}$$

When $\zeta \gg 1$, we can simplify the expression by expanding in powers of ζ^{-1}, and, to leading order, we obtain,

$$F(\zeta) \underset{\zeta \gg 1}{\approx} \frac{\pi}{4\zeta} + \frac{1}{2\zeta^2}(\gamma - 1 - \ln(2\zeta)) - \frac{1}{4\zeta^2}(2\gamma - 1 - 2\ln(2\zeta)), \tag{3.7}$$

where $\gamma \approx 0.577$ is the Euler–Mascheroni constant. Similarly, we also take the other limit $\zeta \ll 1$, where the scaling function approaches a constant value. The dependence of the scaling function F on ζ is plotted in figure 4 and its asymptotic scaling at $\zeta \gg 1$ as $F \sim \zeta^{-1}$ is included as the dotted line. We can discuss the implications of these results better when we use dimensional quantities and write the asymptotic behaviour of the self-propulsion speed as

$$v_x^a \approx \begin{cases} \frac{\pi}{4} \frac{\alpha_0}{\Gamma \ell_d} = \frac{\pi}{4} \frac{\alpha_0 \ell_d}{\eta}, & \zeta \gg 1 \\ \frac{\alpha_0}{\Gamma \xi}, & \zeta \to 0. \end{cases} \tag{3.8}$$

As anticipated from dimensional analysis, $v_x^a \sim (\alpha_0 / \Gamma \xi)$, in the overdamped limit where dissipation is controlled only by frictional drag [23,24,26]. In the underdamped limit, where the effect of drag is much smaller than viscous dissipation, hydrodynamic lengthscale becomes important in screening the divergence of the self-propulsion speed with system size, such that v_x^a scales instead as $v_x^a \sim \alpha_0 / \sqrt{\eta \Gamma}$. In this case, the self-driven motion of $+1/2$ defect is reduced by both friction and viscosity.

As discussed in the introduction, the presence of a finite drag always cuts off the large-scale divergence of the speed of a single defect obtained in a purely viscous two-dimensional layer at the dissipation length ℓ_d. When the flow equations for a thin nematic film of thickness h on a substrate are derived via a lubrication approximation, the effective friction coefficient relates to the film thickness and the viscosity of the substrate bulk fluid (oil), and scales as $\Gamma \sim \bar{\eta}/h^2$ [29]. A more detailed calculation relevant to active microtubule suspensions confined between water and oil shows that the bulk viscosity plays an important role as an additional source of dissipation in the nematic layer affecting the individual defect self-propulsion [30], as well as the vortex statistics in the active turbulence regime [31]. Note that [30] shows that the $+1/2$ defect speed decays algebraically with the bulk oil viscosity (that controls the drag) in the regime where the flow dissipation comes from the viscous dissipation in the nematic layer, consistent with our formulation. When the flow dissipation is dominated by the oil bulk viscosity, there is, however, a logarithmic decay with increasing oil viscosity and, indirectly, drag.
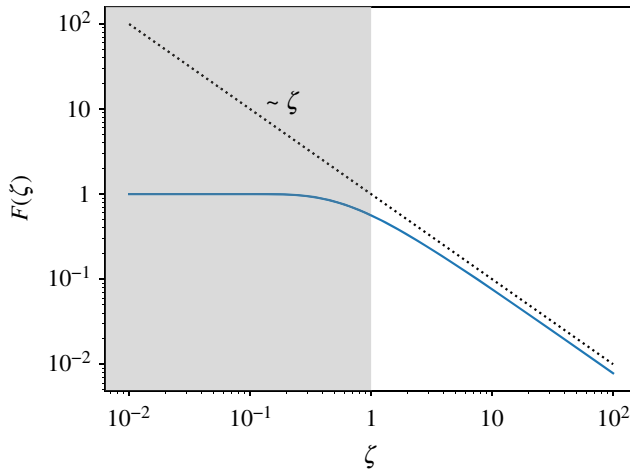
Figure 4. Scaling function $F(\zeta)$ as a function of ζ. The grey region corresponds to the overdamped limit where v_x^a depends only on friction. The dotted black line is the asymptotic limit for $\zeta \gg 1$. (Online version in colour.)

(b) Flow field away from the defect

Outside the core, we treat the defect as a point source. From symmetry considerations, the flow velocity due to σ^a is again non-zero only along the x-direction and it is given by

$$u_x^a(\mathbf{r}) = \frac{\alpha}{2\pi\zeta^2} \int \frac{d\mathbf{r}'}{r'} K_0\left(\frac{|\mathbf{r}' - \mathbf{r}|}{\zeta}\right). \tag{3.9}$$

The flow velocity associated with pressure gradients is finite also in the y-direction and it is given by

$$u_i^p(\mathbf{r}) = -\frac{\alpha}{2\pi\zeta^2} \int d\mathbf{r}' K_0\left(\frac{|\mathbf{r}' - \mathbf{r}|}{\zeta}\right) \left(\frac{\delta_{ix}}{r'} - \frac{x'r_i'}{r'^3}\right). \tag{3.10}$$

The term proportional to the δ function in equation (3.10) cancels $\mathbf{u}_x^a$ from equation (3.9), such that the total active fluid flow is entirely determined by pressure flow, with

$$u_i(\mathbf{r}) = \frac{\alpha}{2\pi\zeta^2} \int d\mathbf{r}' K_0\left(\frac{|\mathbf{r}' - \mathbf{r}|}{\zeta}\right) \frac{x'r_i'}{r'^3}. \tag{3.11}$$

To evaluate this integral, we use a complex representation $u = u_x + iu_y$ and evaluate the resulting contour integrals as shown in appendix A where we express them in terms of complete elliptic integrals of first and second kind. We further use the power series representation of these elliptic integrals, which allows us to write the active fluid velocity as a series expansion in integrals over the zeroth-order modified Bessel function, namely

$$u^+(r, \phi) = \frac{\alpha}{2\zeta^2} \sum_{n=0}^{\infty} \left(1 - \frac{2n+1}{2n-1} e^{2i\phi}\right) \left(\frac{(2n-1)!!}{(2n)!!}\right)^2 \int_0^r dr' K_0\left(\frac{r'}{\zeta}\right) \left(\frac{r'}{r}\right)^{2n+1}$$

$$+ \frac{\alpha}{2\zeta^2} \sum_{n=0}^{\infty} \left(1 - \frac{n}{n+1} e^{2i\phi}\right) \left(\frac{(2n-1)!!}{(2n)!!}\right)^2 \int_r^{\infty} dr' K_0\left(\frac{r'}{\zeta}\right) \left(\frac{r}{r'}\right)^{2n}. \tag{3.12}$$

The $K_0(x)$ integrals are computed in appendix B. After some mathematical manipulations the velocity reduces to

$$u^+(r, \phi) = \frac{\alpha}{4\zeta} \left[\pi \left(I_0\left(\frac{r}{\zeta}\right) - I_2\left(\frac{r}{\zeta}\right) e^{2i\phi}\right)\right.$$

$$\left. + \sum_{k,n=0}^{\infty} (\kappa_1^+(n,k) + \kappa_2^+(n,k)e^{2i\phi}) \frac{1}{(k!)^2} \left(\frac{r}{2\zeta}\right)^{2k+1}\right], \tag{3.13}$$

with

$$\kappa_1^+(n,k) = \left(\frac{(2n-1)!!}{(2n)!!}\right)^2 \left(\frac{-(4n+1)(4k+3)}{(n+k+1)^2(2n-1-2k)^2}\right) \tag{3.14}$$

and

$$\kappa_2^+(n,k) = \left(\frac{(2n-1)!!}{(2n)!!}\right)^2 \frac{[(2n-1)(4k(n+1)+1+n)-4k^2](4n+1)}{(n+1+k)^2(2n-1-2k)^2(n+1)(2n-1)}. \tag{3.15}$$

The corresponding vorticity is given by

$$\omega^+(r,\phi) = -\frac{\alpha}{8\zeta^2}\sin(\phi)\left(4\pi I_1\left(\frac{r}{\zeta}\right) + \sum_{n,k}[(2k+1)\kappa_1^+(n,k)\right.$$

$$\left. -(2k+3)\kappa_2^+(n,k)]\frac{1}{(k!)^2}\left(\frac{r}{2\zeta}\right)^{2k}\right). \tag{3.16}$$

Both velocity and vorticity are shown in figure 1.

(i) Asymptotic far-field flow

The flow field greatly simplifies in the far-field $r/\zeta \gg 1$, corresponding to distances much larger than the hydrodynamic dissipation length. Then, the second term in equation (3.12) vanishes due to the exponential decay of the Bessel function. In the first integral, we can replace the upper limit r with ∞ and perform it analytically with the result given as

$$u^+(r,\phi) = \frac{\alpha}{2r}\left(e^{2i\phi} + 1 + \left(\frac{\zeta}{r}\right)^2(1-3e^{2i\phi})\right), \tag{3.17}$$

where we have kept the two first terms in the expansion. The slow $1/r$-decay term in equation (3.17) is independent of viscosity η and identical to the one derived in Ref. [24] in the friction-dominated regime. Corrections due to viscosity give rise to faster $1/r^3$ decay. The corresponding far-field vorticity is

$$\omega^+(r,\phi) = \frac{\alpha}{r^2}\sin\phi\left(1 + 3\left(\frac{\zeta}{r}\right)^2\right). \tag{3.18}$$

The far-field solutions are singular at the origin, which is not the case for the full series solution that resolves the near core field. This is demonstrated visually in figure 1c,d where we plot cross sections of the velocity and vorticity profiles for both the full solution and the far-field solution. The form of the expressions makes it natural to scale the position, velocity and vorticity with ζ, $\zeta/|\alpha|$ and $\zeta^2/|\alpha|$ respectively. The only free parameter is then the sign of α. Panels (a) and (b) show the flow streamlines and the vorticity field in the background for the full and the far-field solutions, respectively, for an extensile system ($\alpha < 0$). The velocity magnitude is highest near the defect core and decays as a power law following the far-field asymptote. The velocity streamlines point towards the defect in the right half-plane, and away from the defect in the left half-plane. For positive α, the flow direction is reversed. In an infinite system, the flow streamlines around an isolated defect are not closed. On the other hand, as discussed later, in bounded domains, the system size controls the size of the eddies formed around the defect. For more realistic configurations with many defects, the system size is typically replaced by the mean defect separation. It may be that other intrinsic length scales controlled by elastic stresses are also important in stabilizing finite-size vortices. These effects are left for future investigation.

4. Negative nematic defect in an infinite system

By similar calculations as in §3, we find that the velocity induced by the active stress at the position of the negative defect vanishes as expected from symmetry consideration. After performing the integral in the complex plane and subsequently integrating over the integrand with the Bessel

function, we determine the pressure field induced by the $-1/2$ defect vanishes inside the defect core and non-zero outside given by

$$p(\mathbf{r}) = \begin{cases} 0, & r < 1, \\ -\alpha \frac{x^3 - 3xy^2}{3r^3}, & r > 1 \end{cases} \tag{4.1}$$

and its gradient vanishes at the origin, hence no advective pressure-flow of the negative defect. Thus, an isolated $-1/2$ defect is stationary in a uniform nematic field, regardless of activity.

(a) Flow field away from the defect

The flow field induced by the $-1/2$ defect can also be expressed analytically as a series expansion of the elliptic integrals as detailed in appendix C, with the resulting expression of the velocity field in the complex representation $u^- = u_x^- + i u_y^-$ given as

$$u^-(r, \phi) = -\frac{\alpha}{2\zeta^2} \sum_{n=0}^{\infty} \left(\frac{(2n-1)!!}{(2n)!!} \right)^2 \frac{2n+1}{2n-1} \left[e^{4i\phi} \frac{2n+3}{2n-3} - e^{-2i\phi} \right] \int_0^r dr' K_0 \left(\frac{r'}{\zeta} \right) \left(\frac{r'}{r} \right)^{2n+1}$$

$$- \frac{\alpha}{2\zeta^2} \sum_{n=0}^{\infty} \left(\frac{(2n-1)!!}{(2n)!!} \right)^2 \frac{n}{n+1} \left[e^{4i\phi} \frac{n-1}{n+2} - e^{-2i\phi} \right] \int_r^{\infty} dr' K_0 \left(\frac{r'}{\zeta} \right) \left(\frac{r}{r'} \right)^{2n}. \tag{4.2}$$

The integrals over the Bessel functions are evaluated in appendix B, and the final expression is then given as

$$u^-(r, \phi) = \frac{\alpha}{8\zeta} \left(2\pi \left[I_2 \left(\frac{r}{\zeta} \right) e^{-2i\phi} - I_4 \left(\frac{r}{\zeta} \right) e^{4i\phi} \right] \right.$$

$$\left. + \sum_{k,n} [\kappa_1^-(n,k) e^{-2i\phi} + \kappa_2^-(n,k) e^{4i\phi}] \frac{2}{(k!)^2} \left(\frac{r}{2\zeta} \right)^{2k+1} \right) \tag{4.3}$$

with the coefficients

$$\kappa_1^-(n,k) = \left(\frac{(2n-1)!!}{(2n)!!} \right)^2 \frac{(4n+1)[4k^2 - (2n-1)(4k+1)(n+1)]}{(2n-1)(n+1)(n+1+k)^2(2n-1-2k)^2} \tag{4.4}$$

and

$$\kappa_2^-(n,k) = \left(\frac{(2n-1)!!}{(2n)!!} \right)^2 \left[\frac{4n(n-1)}{(n+1)(n+2)(2n-1-2k)^2} \right.$$

$$\left. - \frac{(2n+1)(2n+3)}{(2n-1)(2n-3)(n+k+1)^2} \right]. \tag{4.5}$$

The corresponding vorticity field as function of the polar coordinates follows as:

$$\omega^-(r, \phi) = -\frac{\alpha}{8\zeta^2} \sin(3\phi) \left(4\pi I_3 \left(\frac{r}{\zeta} \right) + \sum_{k,n} [(2k-1)\kappa_1^-(n,k) \right.$$

$$\left. - (2k+5)\kappa_2^-(n,k)] \frac{1}{(k!)^2} \left(\frac{r}{2\zeta} \right)^{2k} \right). \tag{4.6}$$

(b) Asymptotic far-field flow

As with the $+1/2$ defect, the far-field asymptotic flow is dominated by the leading order terms in the expansion, which can also be computed directly from equation (4.2) in the limit of $r/\zeta \to \infty$.
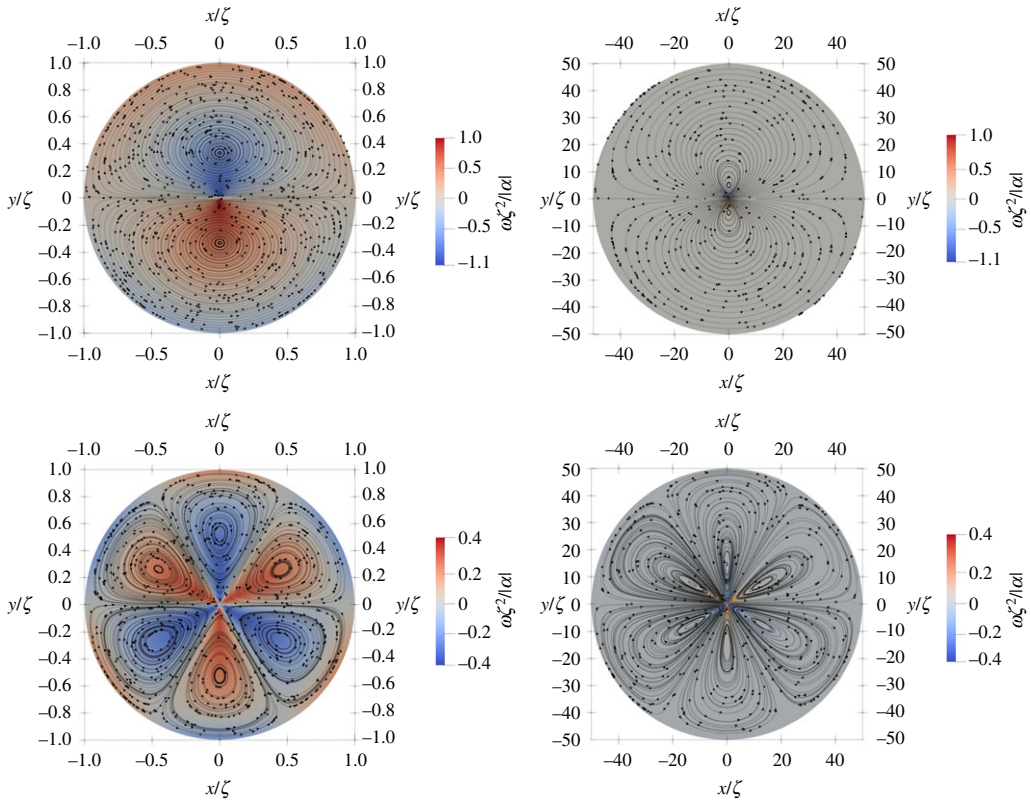
Figure 5. Flow streamlines (black lines) with vorticity as a colour map background generated by a $+1/2$ (a,b) and a $-1/2$ (c,d) defect in discs of different radii R for an extensile system ($\alpha < 0$). (a) and (c) are for $R = 1$ and (b) and (d) $R = 50$. (Online version in colour.)

The result of this calculation is that

$$u^-(r,\phi) \underset{\frac{r}{\zeta} \gg 1}{\approx} = \frac{\alpha}{2r}\left[\left(\frac{\zeta}{r}\right)^2 (15e^{4i\phi} + 3e^{-2i\phi}) - (e^{4i\phi} + e^{-2i\phi})\right]. \tag{4.7}$$

As for equation (3.17) the $1/r$ term here was also obtained in [24]. The vorticity related to this velocity is

$$\omega^-(r,\phi) = \frac{3\alpha \sin(3\phi)}{r^2}\left(5\left(\frac{\zeta}{r}\right)^2 - 1\right). \tag{4.8}$$

In this asymptotic approximation, the flow field is singular at the origin. This singularity is however lifted by the higher order terms in the series expansions, so that the exact flow is smooth everywhere. Figure 2 shows the flow streamlines with the vorticity field as the colour map for the asymptotic (in a) and the exact solutions (in b), with the values scaled in the same way as for figure 1. Cross sections of the vorticity and velocity at $y = 0$ are plotted in (c,d) showing the singular behaviour of the asymptotic approximation at the origin, while it captures very well the far-field behaviour. The plots correspond to an extensile system with $\alpha < 0$. The $\sin(3\phi)$ factor in the vorticity divides the plane in six regions where the sign of the vorticity is altered and making it multi-valued at the origin. The size of the velocity is zero at origin as we discussed above. It increases a bit outside before it starts to decay with increasing r following the far-field asymptotic behaviour.

As for the $+1/2$ defect, the flow streamlines never closed in an infinite system, thus there are no finite size vortices. In the next section, we discuss how the picture changes once the defect is placed in bounded domain.
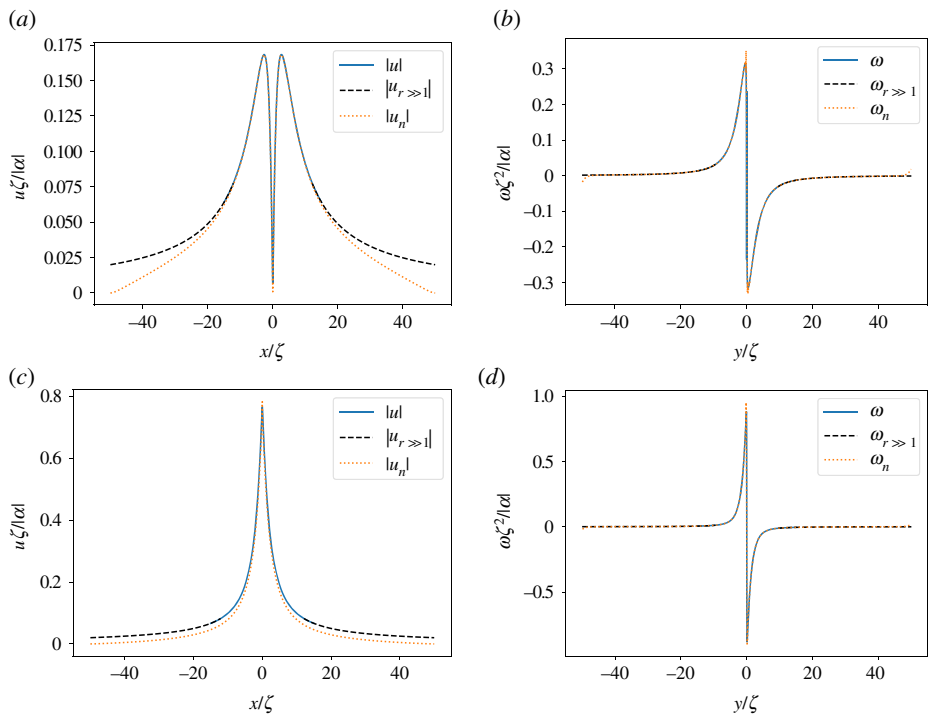
Figure 6. Cross sections of the numerically obtained velocity (a,c) and vorticity (b,d) profiles for $R = 50$ (in units of ℓ_d) (orange dotted lines) are compared with the analytical solution for an infinite system (solid blue lines) for a negative (a,b) and positive (c,d) defect. x and y are also in units of ℓ_d. The dashed black lines are the asymptotic solutions. (Online version in colour.)
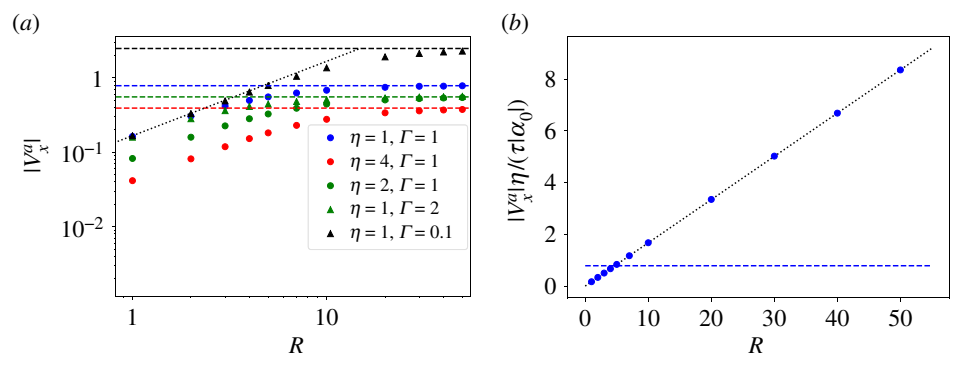

Figure 7. The self-propulsion speed of a $+1/2$ defect as a function of the disc radius, R for (a) different values of the parameters η and Γ and (b) $\Gamma = 0$. The black dotted line is a best fit line for the system in (b), it is also plotted for the $\Gamma \neq 0$ systems ignoring the constant term. Horizontal dashed lines are the analytical prediction for an infinite system $v_+^{(a)} = \pi \alpha_0/(4\sqrt{\eta\tau})$ with the rescaled activity $|\alpha_0| = 1$. (Online version in colour.)

5. Isolated defect in a bounded active nematic

The problem of finding the flow field around defects in a bounded domain is challenging to solve analytically. Thus, we resort to numerical solutions of the Stokes flow given by equation (2.4) in a disc of radius R using finite-element methods and homogeneous boundary conditions (zero velocity). In addition, we use the simplification that a single defect is imprinted in an

uniform nematic field, while the changes in the nematic orientation induced by confinement are ignored [17].

The Stokes flow equation (2.4) is solved with FEniCS using Taylor–Hood elements, which are quadratic for the velocity and linear for the pressure and vorticity [32,33].

Figure 1 shows the flow streamlines induced by a single $+1/2$ (a,b) and $-1/2$ (c,d) defect in a disc of radius R for an extensile system for $\eta \neq 0$ and $\Gamma \neq 0$. The left and right columns correspond to $R = 1$ and $R = 50$, respectively. In a bounded system, the vortical flows around each defect span the system size, as also reported in [17] for $\Gamma = 0$. However, due to friction with the substrate, the flow decays on length scales larger than ℓ_d. This is evident by comparing the values in the far-field of vorticity in the left and right columns from figure 5, corresponding to $R = 1$ (in units of ℓ_d) in (a,c) and $R = 50$ (in units of ℓ_d) in (b,d). We note that the centre of a vortex is not fixed at the maximum of the vorticity. This is due to the fact that the $\pm 1/2$ defects generate shear flows that localize shear vorticity next to the defect cores. However, unlike curvature vorticity in rotating flows which peaks at the vortex core, shear vorticity is not necessarily an indication of the presence of vortices or their location. In fact, with increasing R, the flow gradients near the defect cores become sharper, the streamlines near the cores are 'stretched' in the radial direction, and the eyes of vortices move further from the origin. In the limit $R \to \infty$, we expect vortices to get stretched out so that flow streamlines close at infinity, and we recover the analytic flow profiles.

In figure 6, we compare the cross-sectional profiles of velocity and vorticity obtained from the numerical solution for a large system, $R = 50$ (ℓ_d) to the analytical solutions. The analytical solutions is obtained by truncating the summation in the full solution at $n = 5000$ and $k = 500$ up to $r = 15$ and then using the asymptotic solution for $r > 15$. The plots of velocity in panels (a,c) show that the numerical and analytical solutions agree very well close to the defect cores, but deviate from each other near the boundary. This is due to the imposed boundary conditions of the vanishing velocity field. The vorticity in panels (b,d) agrees well in the entire domain, with a small boundary effect due to vanishing velocity and vortices spanning the system size. This effect is perhaps more visible for the negative defect and decreases with increasing R.

The self-propulsion speed v_x^a of the $+1/2$ defect is also affected by the system size. If $\Gamma = 0$ at the outset $v_x^a \sim R$, as noted in [17]. Frictional damping screens out this divergence, yielding the finite value given in equation (3.7) for $R \to \infty$. The numerical calculation shows, however, that for smaller R there are finite-size corrections to the defect propulsive speed. These are displayed in figure 7, where we plot $|v_x^a|$ as a function of R obtained from the numerical solution of equation (2.4) for different values of η and Γ. The horizontal dashed lines are the analytical solution in the limit of an infinite system, as given by $v_x^{(a)} \approx (\pi/4)(\alpha_0/\sqrt{\eta \Gamma})$, while the dotted black lines show the linear scaling with R in the limit of zero friction. We note that viscosity η determines the slope for R dependence in small systems, while friction Γ controls the cross-over to the intrinsic constant speed. Note that the asymptotic constant values of v_x^a agree very well with the analytical prediction at $\zeta \gg 1$ because in the numerical computations the vortex core is actually set to zero (hydrodynamic regime with $S = 1$). For comparison, we also show in figure 7b the defect propulsion speed in the absence of friction $\Gamma = 0$ from the outset, where the speed increases linearly with the system size. The dotted black line represents the analytical prediction as found in [17].

6. Conclusion

In summary, we have evaluated the flow field induced by an isolated $\pm 1/2$ defect in an incompressible active nematic film on a substrate both for an infinite system and a finite-size disc. While the self-propulsion speed of a $+1/2$ defect diverges with system size for an isolated film, we show analytically that the presence of finite substrate friction Γ cures this divergence resulting in a finite speed $v_x^{(a)} \approx (\pi/4)(\alpha_0/\sqrt{\eta \Gamma}) = (\pi/4)(\alpha_0/\eta)\ell_d$ that increases with the hydrodynamic dissipation length ℓ_d. This is also confirmed numerically in a finite disc with $R > \ell_d$. For small discs with $R < \ell_d$, the active speed scales instead linearly with R.

Stable shear vortical flows are formed around the defects. In finite systems, the size of the flow vortices is controlled by the dissipation length ℓ_d, hence spans the whole system if $\ell_d > R$. The eye of the vortices shifts away from the defect core with increasing R. For infinite-size systems, the flow streamlines close at infinity as predicted by the far-field analytical solution. In the same limit, we showed that the absolute value of the velocity decreases as $1/r$ for distances that are large compared with the dissipation length scale, in agreement with previous studies. The $1/r$ far-field decay of the flow created by defects may seem surprising as it suggests that a defect acts like a point force. This behaviour arises from the long-range nature of the distortion of the texture created by defects. When other defects are present (as required in the plane to guarantee zero net topological charge), this decay is cut off by the defect separation. In finite domains, it is cut off by the system size. The $1/r$ decay indicates, however, that a multi-defect approach is needed to describe the defect gas, as attempted in [34,35].

In this work, we have neglected the effect of the elastic stress. An interesting extension would be to study the effects it would have on the flow field, and also considering the effect of having multiple interacting defects.

Appendix A. Integrals for the $+1/2$ defect

Here, we provide the detailed steps that are taken to arrive at equation (3.12) from equation (3.11). We start by changing to a complex representation $u = u_x + iu_y$ with complex coordinates $z = x + iy$ and $z' = x' + iy'$. By changing variables to $t = z' - z$, and then to polar coordinates $t = r'e^{i\theta} = r'\hat{z}$, we write equation (3.11) as

$$u = \frac{\alpha}{4i\pi\zeta^2} \int dr' r' K_0\left(\frac{r'}{\zeta}\right) \oint_\gamma d\hat{z}$$
$$\times \left(\frac{r'\hat{z}^2 + z\hat{z}}{(r' + \bar{z}\hat{z})\sqrt{\hat{z}(r'\hat{z} + z)(r' + \bar{z}\hat{z})}} + \frac{1}{\sqrt{\hat{z}(r'\hat{z} + z)(r' + \bar{z}\hat{z})}} \right), \tag{A 1}$$

where γ is the unit circle. We note that the integral over $\hat{z}$ is over three branch points. $\hat{z} = 0$ is always in the unit circle, $\hat{z} = -z/r$ is inside when $|z| < r$ and $\hat{z} = -r/\bar{z}$ when $|z| > r$. We consider the integral over $\hat{z}$ and start by looking at the last term. Splitting up the square root, we write it as

$$\frac{1}{\sqrt{\bar{z}r'}} \oint_\gamma d\hat{z} \frac{1}{\sqrt{\hat{z}}\sqrt{\left(\hat{z} + \frac{z}{r'}\right)}\sqrt{\left(\hat{z} + \frac{r'}{\bar{z}}\right)}}. \tag{A 2}$$

We see that for all values of r' we have two branch points inside of the contour. Therefore, we write the integral as

$$\frac{1}{\sqrt{\bar{z}r'}} \oint_\gamma d\hat{z} \frac{1}{\sqrt{\hat{z}}\sqrt{(\hat{z} + a)}\sqrt{(\hat{z} + b)}}. \tag{A 3}$$

From here, $-a$ is the branch point inside of the contour, while $-b$ is the point outside of the contour. We note that the complex numbers a and b have the same argument ϕ so we can write it
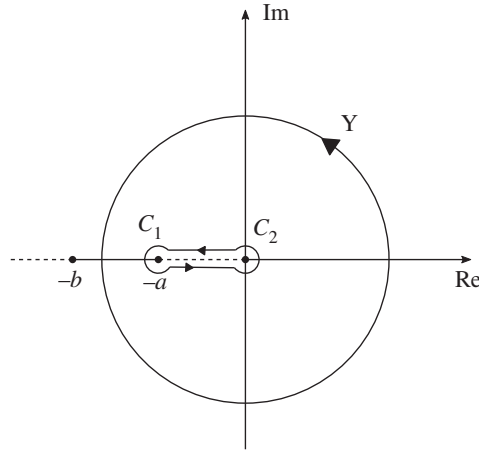
Figure 8. Sketch of the keyhole contour in the complex plane associated with the integral in equation (A 4).

as

$$\frac{1}{\sqrt{\bar{z}r'}} \oint_\gamma \mathrm{d}\hat{z} \frac{1}{\sqrt{\hat{z}}\sqrt{(\hat{z}+a\mathrm{e}^{\mathrm{i}\phi})}\sqrt{(\hat{z}+b\mathrm{e}^{\mathrm{i}\phi})}}. \tag{A 4}$$

a and b are now either r/r' and r'/r. If we change our integral variable from $\hat{z}$ to $\hat{u} = \hat{z}\mathrm{e}^{-\mathrm{i}\phi}$, we get

$$\frac{1}{\sqrt{\bar{z}r'}} \oint_\gamma \mathrm{d}\hat{u}\mathrm{e}^{\mathrm{i}\phi} \frac{1}{\sqrt{\mathrm{e}^{\mathrm{i}\phi}\hat{u}}\sqrt{(\mathrm{e}^{\mathrm{i}\phi}\hat{u}+a\mathrm{e}^{\mathrm{i}\phi})}\sqrt{(\mathrm{e}^{\mathrm{i}\phi}\hat{u}+b\mathrm{e}^{\mathrm{i}\phi})}}$$

$$= \frac{\mathrm{e}^{-\mathrm{i}\phi/2}}{\sqrt{\bar{z}r'}} \oint_\gamma \mathrm{d}\hat{u} \frac{1}{\sqrt{\hat{u}}\sqrt{(\hat{u}+a)}\sqrt{(\hat{u}+b)}}. \tag{A 5}$$

Note that all branch points $\hat{z}=0$, $-a$ and $-b$ are now located on the real axis. We now have to consider what branch cuts we want to use to perform this integral. We consider the integral over the domain as shown in figure 8. Here, we have cut out a area around the branch cut in order to avoid problems. The key hole consists of a circle C_1 with radius ϵ around $-a$, the circle C_2 around the origin and the lines connecting them which is ϵ above or below the real line as shown in figure 8. Since there are no poles in the domain between the two contours, the integral of them has to be the same [36]. The contour integral becomes

$$\int_\gamma \frac{\mathrm{e}^{-\mathrm{i}\phi/2}}{\sqrt{\bar{z}r'}} \mathrm{d}\hat{u} \frac{1}{\sqrt{\hat{u}}\sqrt{(\hat{u}+a)}\sqrt{(\hat{u}+b)}}$$

$$= \left(\int_{-a-\mathrm{i}\epsilon \to -\mathrm{i}\epsilon} + \int_{\mathrm{i}\epsilon \to -a+\mathrm{i}\epsilon} + \int_{C_1} + \int_{C_2} \right) \frac{\mathrm{e}^{-\mathrm{i}\phi/2}}{\sqrt{\bar{z}r'}} \frac{\mathrm{d}\hat{u}}{\sqrt{\hat{u}}\sqrt{(\hat{u}+a)}\sqrt{(\hat{u}+b)}}. \tag{A 6}$$

When $\epsilon \to 0$, the integrals over C_1 and C_2 disappears. The integral above the real line is just above the branch cut and therefore positive, while the one below is negative. We therefore get

$$\oint_\gamma \frac{\mathrm{e}^{-\mathrm{i}\phi/2}}{\sqrt{\bar{z}r'}} \mathrm{d}\hat{u} \frac{1}{\sqrt{\hat{u}}\sqrt{(\hat{u}+a)}\sqrt{(\hat{u}+b)}} = -2\frac{\mathrm{e}^{-\mathrm{i}\phi/2}}{\sqrt{\bar{z}r'}} \int_{-a}^0 \mathrm{d}\hat{u} \frac{1}{\sqrt{\hat{u}}\sqrt{(\hat{u}+a)}\sqrt{(\hat{u}+b)}}. \tag{A 7}$$

Evaluating this integral, we obtain

$$\oint_\gamma \frac{\mathrm{e}^{-\mathrm{i}\phi/2}}{\sqrt{\bar{z}r'}} \mathrm{d}\hat{u} \frac{1}{\sqrt{\hat{u}}\sqrt{(\hat{u}+a)}\sqrt{(\hat{u}+b)}} = 4\mathrm{i}\frac{\mathrm{e}^{-\mathrm{i}\phi/2}}{\sqrt{\bar{z}r'}} \frac{1}{\sqrt{b}} K\left(\frac{a}{b}\right). \tag{A 8}$$

Here, K is the complete elliptic integral of the first kind with the power series

$$K(x) = \frac{\pi}{2} \sum_{n=0}^{\infty} \left(\frac{(2n-1)!!}{(2n)!!} \right)^2 x^n. \tag{A 9}$$

With the double factorial $(2n)!! = 2 \cdot 4 \cdot 6 \cdots (2n-2) \cdot 2n$.

We now consider the other integral over $\hat{z}$ in equation (A 1):

$$\oint_\gamma d\hat{z} \frac{r'\hat{z}^2 + z\hat{z}}{(r' + \bar{z}\hat{z})\sqrt{\hat{z}(r'\hat{z} + z)(r' + \bar{z}\hat{z})}}. \tag{A 10}$$

This is not symmetric in the branch points as the other integral was. We can write this as

$$r'^{1/2}\bar{z}^{-3/2} \oint_\gamma d\hat{z} \frac{\hat{z}^{1/2}(\hat{z} + e^{i\phi}r/r')^{1/2}}{(\hat{z} + e^{i\phi}r'/r)^{3/2}}, \tag{A 11}$$

and we can rotate the integral variable to $u = \hat{z}e^{-i\phi}$ and get

$$r'^{1/2}\bar{z}^{-3/2} \oint_\gamma d\hat{u}e^{i\phi} \frac{\hat{u}^{1/2}e^{i\phi/2}(\hat{u}e^{i\phi} + e^{i\phi}r/r')^{1/2}}{(\hat{u}e^{i\phi} + e^{i\phi}r'/r)^{3/2}}$$

$$= r'^{1/2}\bar{z}^{-3/2}e^{i\phi/2} \oint_\gamma d\hat{u} \frac{\hat{u}^{1/2}(\hat{u} + r/r')^{1/2}}{(\hat{u} + r'/r)^{3/2}}. \tag{A 12}$$

Which of the branch points that are inside of the integral depends on the value of r'. If $r' > r$ then r/r' is inside of the units circle. We can then use the same branch cuts and arguments as before and find

$$r'^{1/2}\bar{z}^{-3/2}e^{i\phi/2} \oint_\gamma d\hat{u} \frac{\hat{u}^{1/2}(\hat{u} + r/r')^{1/2}}{(\hat{u} + r'/r)^{3/2}}$$

$$= -2r'^{1/2}\bar{z}^{-3/2}e^{i\phi/2} \int_{-r/r'}^{0} d\hat{u} \frac{\hat{u}^{1/2}(\hat{u} + r/r')^{1/2}}{(\hat{u} + r'/r)^{3/2}}. \tag{A 13}$$

We can perform the integral and find that it equals

$$- 2r'^{1/2}\bar{z}^{-3/2}e^{i\phi/2} \frac{2i}{\sqrt{r'/r}} \left[\left(\frac{2r'}{r} - \frac{r}{r'} \right) K\left(\frac{r^2}{r'^2} \right) - \frac{2r'}{r} E\left(\frac{r^2}{r'^2} \right) \right]. \tag{A 14}$$

Here, $E(x)$ is the complete elliptic integral of the second kind with the power series

$$E(x) = \frac{\pi}{2} \left(1 - \sum_{n=1}^{\infty} \left(\frac{(2n-1)!!}{(2n)!!} \right)^2 \frac{x^n}{2n-1} \right). \tag{A 15}$$

The other possibility is that $r' < r$. Now it is the $-3/2$ root that is inside of the integral domain. In this case, we cannot use the above approach since the integrand does not go to zero when $\hat{z}$ goes to r'/r. However, we can use the binomial expansion that is valid for $|x| < 1$. We have that

$$r'^{1/2}\bar{z}^{-3/2}e^{i\phi/2} \oint_\gamma d\hat{u} \frac{\hat{u}^{1/2}(\hat{u} + a)^{1/2}}{(\hat{u} + b)^{3/2}}. \tag{A 16}$$

Doing a change of variables to $h = \sqrt{u}$ with $dh = du/(2\sqrt{u})$. We then get (remembering a factor half since because integrating once around h we have gone twice around u)

$$r'^{1/2}\bar{z}^{-3/2}e^{i\phi/2} \oint_\gamma dh \frac{h^2(h^2 + a)^{1/2}}{(h^2 + b)^{3/2}}. \tag{A 17}$$

We have that $|h| = 1$, $a > 1$ and $b < 1$. We therefore write this

$$r'^{1/2}\bar{z}^{-3/2}e^{i\phi/2} \oint_\gamma dh \frac{\sqrt{a}(1 + h^2/a)^{1/2}}{h(1 + b/h^2)^{3/2}}. \tag{A 18}$$

We now use the binomial expansion

$$(1 + x)^r = \sum_{n=0}^{\infty} \binom{r}{n} x^n, \tag{A 19}$$

and the integral becomes

$$r'^{1/2} \bar{z}^{-3/2} e^{i\phi/2} \sqrt{a} \oint_\gamma \frac{dh}{h} \left(\sum_{n=0}^{\infty} \binom{1/2}{n} \left(\frac{h^2}{a}\right)^n \right) \left(\sum_{k=0}^{\infty} \binom{-3/2}{k} \left(\frac{b}{h^2}\right)^k \right). \tag{A 20}$$

By the residue theorem only the terms where $k = n$ is contributing to the integral. We therefore get

$$r'^{1/2} \bar{z}^{-3/2} e^{i\phi/2} \sqrt{a} \oint_\gamma \frac{dh}{h} \left(\sum_{n=0}^{\infty} \binom{1/2}{n} \binom{-3/2}{n} \left(\frac{b}{a}\right)^n \right)$$

$$= 2\pi i r'^{1/2} \bar{z}^{-3/2} e^{i\phi/2} \sqrt{a} \left(\sum_{n=0}^{\infty} \binom{1/2}{n} \binom{-3/2}{n} \left(\frac{b}{a}\right)^n \right). \tag{A 21}$$

Inserting the expressions for a and b, we find

$$2\pi i \bar{z}^{-3/2} e^{i\phi/2} \sqrt{r} \sum_{n=0}^{\infty} \binom{1/2}{n} \binom{-3/2}{n} \left(\frac{r'}{r}\right)^{2n}. \tag{A 22}$$

Now we have solved the integral over the angles $\hat{z}$. Inserting this into the equation (A1), we find

$$u = \frac{\alpha}{4i\pi \zeta^2} \int_0^r dr' r' K_0(r'/\zeta) \left(2\pi i \bar{z}^{-3/2} e^{i\phi/2} \sqrt{r} \sum_{n=0}^{\infty} \binom{1/2}{n} \binom{-3/2}{n} \left(\frac{r'}{r}\right)^{2n} \right.$$

$$+ \frac{4i e^{-i\phi/2}}{\sqrt{\bar{z} r'}} \sqrt{\frac{r'}{r}} K\left(\frac{r'^2}{r^2}\right) \right) + \frac{\alpha}{4i\pi \zeta^2} \int_r^\infty dr' r' K_0(r'/\zeta)$$

$$\times \left(\frac{4i e^{i\phi/2} \sqrt{r}}{\bar{z}^{3/2}} \left[\left(\frac{r}{r'} - 2\frac{r'}{r}\right) K\left(\frac{r^2}{r'^2}\right) + 2\frac{r'}{r} E\left(\frac{r^2}{r'^2}\right) \right] \right.$$

$$+ \frac{4i e^{-i\phi/2}}{\sqrt{\bar{z} r'}} \sqrt{\frac{r}{r'}} K\left(\frac{r^2}{r'^2}\right) \right) \tag{A 23}$$

Using that $\bar{z} = r e^{-i\phi}$ and inserting the expressions for the K and E this becomes

$$u = \frac{\alpha}{2\zeta^2} \int_0^r dr' K_0\left(\frac{r'}{\zeta}\right) \left(\frac{r'}{r}\right)^{2n+1} \left(e^{2i\phi} \sum_{n=0}^{\infty} \binom{1/2}{n} \binom{-3/2}{n} + \sum_{n=0}^{\infty} \left(\frac{(2n-1)!!}{(2n)!!}\right)^2 \right)$$

$$+ \frac{\alpha}{2\zeta^2} \int_r^\infty dr' K_0\left(\frac{r'}{\zeta}\right) \left(\frac{r}{r'}\right)^{2n} \left(\sum_{n=0}^{\infty} \left[\left(\frac{(2n-1)!!}{(2n)!!}\right)^2 - 2\left(\frac{(2n+1)!!}{(2n+2)!!}\right)^2 \frac{2n+2}{2n+1} \right] e^{2i\phi} \right.$$

$$+ \sum_{n=0}^{\infty} \left(\frac{(2n-1)!!}{(2n)!!}\right)^2 \right). \tag{A 24}$$

We can simplify this by using that

$$\sum_{n=0}^{\infty} \left(\frac{(2n-1)!!}{(2n)!!}\right)^2 - 2\left(\frac{(2n+1)!!}{(2n+2)!!}\right)^2 \frac{2n+2}{2n+1} = -\sum_{n=0}^{\infty} \left(\frac{(2n-1)!!}{(2n)!!}\right)^2 \frac{n}{n+1}, \tag{A 25}$$

and for the binomial

$$\binom{1/2}{n} \binom{-3/2}{n} = -\frac{2n+1}{2n-1} \left(\frac{(2n-1)!!}{(2n)!!}\right)^2. \tag{A 26}$$

Inserting this we finally arrive at

$$u = \frac{\alpha}{2\zeta^2} \sum_{n=0}^{\infty} \left(\frac{(2n-1)!!}{(2n)!!} \right)^2 \left(1 - \frac{2n+1}{2n-1} e^{2i\phi} \right) \int_0^r dr' K_0 \left(\frac{r'}{\zeta} \right) \left(\frac{r'}{r} \right)^{2n+1}$$

$$+ \frac{\alpha}{2\zeta^2} \sum_{n=0}^{\infty} \left(\frac{(2n-1)!!}{(2n)!!} \right)^2 \left(1 - \frac{n}{n+1} e^{2i\phi} \right) \int_r^{\infty} dr' K_0 \left(\frac{r'}{\zeta} \right) \left(\frac{r}{r'} \right)^{2n}. \tag{A 27}$$

Appendix B. Integrals over the Bessel function

We start a change of variables to $r'' = \zeta^{-1} r'$, and then evaluate the integrals over the Bessel functions as

$$\zeta^{2n+2} \int_0^{r/\zeta} dr'' K_0(r'') r''^{2n+1}$$

$$= \frac{1}{4} r^{2n+2} n! \left[n!_2 \tilde{F}_3 \left(1+n, 1+n; 1, 2+n, 2+n; \frac{r^2}{4\zeta^2} \right) \right.$$

$$- 2_1 \tilde{F}_2 \left(1+n; 1, 2+n; \frac{r^2}{4\zeta^2} \right) \left(\gamma + \ln \left(\frac{r}{2\zeta} \right) \right)$$

$$\left. + 2 \frac{\partial}{\partial a_1} {}_2\tilde{F}_3 \left(a_1, 1+n; 1, 1, 2+n; \frac{r^2}{4\zeta^2} \right) |_{a_1=1} \right]$$

$$= \frac{1}{4} r^{2n+2} F^{r' < r} \left(n, \frac{r}{\zeta} \right) \tag{B 1}$$

and

$$\zeta^{1-2n} \int_{r/\zeta}^{\infty} dr' K_0(r') \left(\frac{1}{r'} \right)^{2n}$$

$$= \frac{1}{4} r^{-2n+1} \Gamma \left(\frac{1}{2} - n \right) \left[4^{-n} \Gamma \left(\frac{1}{2} - n \right) \left(2 \left(\frac{r}{\zeta} \right)^{2n-1} \right. \right.$$

$$\left. - 4^n {}_2\tilde{F}_3 \left(\frac{1}{2} - n, \frac{1}{2} - n; 1, \frac{3}{2} - n, \frac{3}{2} - n; \frac{r^2}{4\zeta^2} \right) \right)$$

$$+ 2_1 \tilde{F}_2 \left(\frac{1}{2} - n; 1, \frac{3}{2} - n; \frac{r^2}{4\zeta^2} \right) \left(\gamma + \ln \left(\frac{r}{2\zeta} \right) \right)$$

$$\left. - 2 \frac{\partial}{\partial a_1} {}_2\tilde{F}_3 \left(a_1, \frac{1}{2} - n; 1, 1, \frac{3}{2} - n; \frac{r^2}{4\zeta^2} \right) |_{a_1=1} \right]$$

$$= \frac{1}{4} r^{-2n+1} F^{r' > r} \left(n, \frac{r}{\zeta} \right). \tag{B 2}$$

Here, the regularized hypergeometric function is defined as

$$_p\tilde{F}_q(a_1, \ldots, a_p; b_1, \ldots, b_q; x) = \frac{1}{\Gamma(b_1) \cdots \Gamma(b_q)} \sum_{k=0}^{\infty} \frac{(a_1)_k \cdots (a_p)_k}{(b_1)_k \cdots (b_q)_k} \frac{x^k}{k!}, \tag{B 3}$$

where $(a)_k = a \cdot (a+1) \cdots (a+k-1)$ is the rising factorial. These expressions can be simplified. Using that $\Gamma(x) = (x-1)\Gamma(x-1)$, it follows that the Pochhammer symbol is given as

$$(a)_k = \frac{\Gamma(a+k)}{\Gamma(a)}, \tag{B 4}$$

with the derivative

$$\partial_a(a)_k|_{a=1} = (a)_k(\psi^{(0)}(a+k) - \psi^{(0)}(a))|_{a=1} = k!(\psi^{(0)}(1+k) - \psi^{(0)}(1)). \tag{B5}$$

Here, $\psi^{(0)}(k)$ is the digamma function, that is the first derivative of the logarithm of the gamma function. For integer arguments, it is given as

$$\psi^{(0)}(n) = -\gamma + \sum_{l=1}^{n-1} \frac{1}{l}. \tag{B6}$$

Using the relations above, we find after some algebra that the moments are given by the power series

$$F^{r'<r}\left(n, \frac{r}{\zeta}\right) = \sum_{k=0}^{\infty} \left[\frac{1}{(n+k+1)} - 2\left(\gamma + \ln\left(\frac{r}{2\zeta}\right)\right) + 2\sum_{l=1}^{k} \frac{1}{l} \right]$$

$$\times \frac{1}{(n+k+1)(k!)^2} \left(\frac{r}{2\zeta}\right)^{2k} \tag{B7}$$

and

$$F^{r'>r}\left(n, \frac{r}{\zeta}\right) = 4\sum_{k=0}^{\infty} \left[\sum_{l=1}^{k} \frac{1}{l} - \left(\gamma + \ln\left(\frac{r}{2\zeta}\right)\right) - \frac{1}{2n-1-2k} \right] \frac{1}{(2n-1-2k)(k!)^2}$$

$$\times \left(\frac{r}{2\zeta}\right)^{2k} + \frac{2\pi}{((2n-1)!!)^2} \left(\frac{r}{\zeta}\right)^{2n-1}. \tag{B8}$$

Appendix C. Integrals for the $-1/2$ defect

Here, we provide details of the calculation leading to equation (4.2). Using the complex representation with similar coordinate transformations as for the $+1/2$-defect, the corresponding active flow velocity, $u^- = u_x^- + iu_y^-$ induced by active stress and pressure gradient from equation (2.7) reads as

$$u^- = -\frac{\alpha}{4i\pi\zeta^2} \int dr' r' K_0\left(\frac{r'}{\zeta}\right) \oint_\gamma \frac{d\hat{z}}{\hat{z}} \left(\frac{1}{r'\hat{z}+z} \sqrt{\frac{r'\hat{z}^{-1}+\bar{z}}{r'\hat{z}+z}} + \frac{r'\hat{z}+z}{(r'\hat{z}^{-1}+\bar{z})^2} \sqrt{\frac{r'\hat{z}+z}{r'\hat{z}^{-1}+\bar{z}}} \right). \tag{C1}$$

We start by looking at the integral over $\hat{z}$ and we will first consider the second term:

$$\oint_\gamma \frac{d\hat{z}}{\hat{z}} \frac{r'\hat{z}+z}{(r'\hat{z}^{-1}+\bar{z})^2} \sqrt{\frac{r'\hat{z}+z}{r\hat{z}^{-1}+\bar{z}}} = \frac{r'^{3/2}}{\bar{z}^{5/2}} \oint_\gamma d\hat{z} \frac{\hat{z}^{3/2}(\hat{z}+z/r')^{3/2}}{(\hat{z}+r'/\bar{z})^{5/2}}. \tag{C2}$$

Using that $z = re^{i\phi}$ and changing variable to $u = e^{i\phi}\hat{z}$ we get

$$\frac{r'^{3/2}}{\bar{z}^{5/2}} \oint_\gamma d\hat{z} \frac{\hat{z}^{3/2}(\hat{z}+e^{i\phi}r/r')^{3/2}}{(\hat{z}+e^{i\phi}r'/r)^{5/2}} = \frac{r'^{3/2}}{r^{5/2}} e^{4i\phi} \oint_\gamma du \frac{u^{3/2}(u+(r/r'))^{3/2}}{(u+(r'/r))^{5/2}}. \tag{C3}$$

This integral has three branch points on the real axis. Two of these points are inside the integration domain and give troubles. If $r' > r$ we have the two points $u = 0$ and $u = r/r'$ inside of the unit circle. In this case, one uses the same key hole contour technique as (A7) and gets

$$\frac{r'^{3/2}}{r^{5/2}} e^{4i\phi} \oint_\gamma du \frac{u^{3/2}(u+(r/r'))^{3/2}}{(u+(r'/r))^{5/2}} = -2\frac{r'^{3/2}}{r^{5/2}} e^{4i\phi} \int_{-r/r'}^{0} du \frac{u^{3/2}(u+(r/r'))^{3/2}}{(u+(r'/r))^{5/2}}. \tag{C4}$$

Performing this integral, we arrive at

$$\frac{4i}{3} e^{4i\phi} \frac{r'}{r^2} \left(\left[3\left(\frac{r}{r'}\right)^2 - 16 + 16\left(\frac{r'}{r}\right)^2 \right] K\left(\frac{r^2}{r'^2}\right) + \left[8 - 16\left(\frac{r'}{r}\right)^2 \right] E\left(\frac{r^2}{r'^2}\right) \right), \tag{C5}$$

where the functions K and E are defined in appendix A. Now let us look at the integral when $r' < r$. In this case, we can not use the contour approach because the integrand diverges near the r'/r pole. We, therefore, use the binomial expansion to evaluate this integral. We first change the variable to $h = \sqrt{u}$. The integral is then

$$
\frac{r'^{3/2}}{r^{5/2}} e^{4i\phi} \oint_\gamma du \frac{u^{3/2}(u + (r/r'))^{3/2}}{(u + (r'/r))^{5/2}} = \frac{r'^{3/2}}{r^{5/2}} e^{4i\phi} \oint_\gamma dh \frac{h^4(h^2 + a)^{3/2}}{(h^2 + b)^{5/2}}. \tag{C6}
$$

We have introduced $a = r/r'$ and $b = r'/r$ and $|h| = 1$, $|b| < 1$ and $|a| > 1$. We therefore write this as

$$
\frac{r'^{3/2}}{r^{5/2}} a^{3/2} e^{4i\phi} \oint_\gamma dh \frac{h^4(1 + h^2/a)^{3/2}}{h^5(1 + b/h^2)^{5/2}}
$$

$$
= \frac{1}{r} e^{4i\phi} \oint_\gamma \frac{dh}{h} \left(\sum_{k=0}^\infty \binom{3/2}{k} \left(\frac{h^2}{a} \right)^k \right) \left(\sum_{n=0}^\infty \binom{-5/2}{n} \left(\frac{b}{h^2} \right)^n \right). \tag{C7}
$$

The residual theorem makes it so that only the terms with $k = n$ is relevant. The integral finally becomes

$$
\frac{2\pi i}{r} e^{4i\phi} \sum_{n=0}^\infty \binom{3/2}{n} \binom{-5/2}{n} \left(\frac{r'}{r} \right)^{2n}. \tag{C8}
$$

We now turn to the first term in the integral over $\hat{z}$ in equation (C1). It is

$$
\oint_\gamma \frac{d\hat{z}}{\hat{z}} \frac{1}{r'\hat{z} + z} \sqrt{\frac{r'\hat{z}^{-1} + \bar{z}}{r'\hat{z} + z}}. \tag{C9}
$$

We change variables to $t = 1/\hat{z}$ with $dt = -d\hat{z}/\hat{z}^2$. In addition there comes a negative sign because we must reverse the contour. This integral is then

$$
\oint_\gamma \frac{dt}{t} \frac{1}{r't^{-1} + z} \sqrt{\frac{r't + \bar{z}}{r't^{-1} + z}}, \tag{C10}
$$

which is same integral as in equation (A10) with z and $\bar{z}$ interchanged. We can therefore use the solution we found in appendix A with $\phi \to -\phi$. The velocity field is then

$$
u = -\frac{\alpha}{4i\pi\zeta^2} \int_0^r dr' r' K_0 \left(\frac{r'}{\zeta} \right) \left\{ \frac{2\pi i}{r} e^{4i\phi} \sum_{n=0}^\infty \binom{3/2}{n} \binom{-5/2}{n} \left(\frac{r'}{r} \right)^{2n} \right.
$$

$$
+ \frac{2\pi i}{r} e^{-2i\phi} \sum_{n=0}^\infty \binom{1/2}{n} \binom{-3/2}{n} \left(\frac{r'}{r} \right)^{2n} \Bigg\}
$$

$$
- \frac{\alpha}{4i\pi\zeta^2} \int_r^\infty dr' r' K_0 \left(\frac{r'}{\zeta} \right) \left\{ \frac{4i}{3} e^{4i\phi} \frac{r'}{r^2} \left(\left[3 \left(\frac{r}{r'} \right)^2 - 16 + 16 \left(\frac{r'}{r} \right)^2 \right] K \left(\frac{r^2}{r'^2} \right) \right. \right.
$$

$$
\left. + \left[8 - 16 \left(\frac{r'}{r} \right)^2 \right] E \left(\frac{r^2}{r'^2} \right) \right) + 4i e^{-2i\phi} \frac{1}{r} \left[\left(\frac{r}{r'} - 2\frac{r'}{r} \right) K \left(\frac{r^2}{r'^2} \right) + \frac{2r'}{r} E \left(\frac{r^2}{r'^2} \right) \right] \Bigg\}. \tag{C11}
$$

Inserting the expressions for K and E, and using equation (A26) and

$$
\sum_{n=0}^\infty \binom{3/2}{n} \binom{-5/2}{n} = \frac{(2n+1)(2n+3)}{(2n-1)(2n-3)} \left(\frac{(2n-1)!!}{(2n)!!} \right)^2. \tag{C12}
$$

We finally arrive at

$$
u^-(r, \phi) = -\frac{\alpha}{2\zeta^2} \sum_{n=0}^\infty \left(\frac{(2n-1)!!}{(2n)!!} \right)^2 \frac{2n+1}{2n-1} \left[e^{4i\phi} \frac{2n+3}{2n-3} - e^{-2i\phi} \right] \int_0^r dr' K_0 \left(\frac{r'}{\zeta} \right) \left(\frac{r'}{r} \right)^{2n+1}
$$

$$
- \frac{\alpha}{2\zeta^2} \sum_{n=0}^\infty \left(\frac{(2n-1)!!}{(2n)!!} \right)^2 \frac{n}{n+1} \left[e^{4i\phi} \frac{n-1}{n+2} - e^{-2i\phi} \right] \int_r^\infty dr' K_0 \left(\frac{r'}{\zeta} \right) \left(\frac{r}{r'} \right)^{2n}. \tag{C13}
$$

References

1. Sanchez T, Chen DT, DeCamp SJ, Heymann M, Dogic Z. 2012 Spontaneous motion in hierarchically assembled active matter. *Nature* **491**, 431–434. (doi:10.1038/nature11591)
2. Guillamat P, Ignés-Mullol J, Sagués F. 2017 Taming active turbulence with patterned soft interfaces. *Nat. Commun.* **8**, 1–8. (doi:10.1038/s41467-017-00617-1)
3. Needleman D, Dogic Z. 2017 Active matter at the interface between materials science and cell biology. *Nat. Rev. Mater.* **2**, 1–14. (doi:10.1038/natrevmats.2017.48)
4. Kumar N, Zhang R, De Pablo JJ, Gardel ML. 2018 Tunable structure and dynamics of active liquid crystals. *Sci. Adv.* **4**, eaat7779. (doi:10.1126/sciadv.aat7779)
5. Doostmohammadi A, Ignés-Mullol J, Yeomans JM, Sagués F. 2018 Active nematics. *Nat. Commun.* **9**, 1–13. (doi:10.1038/s41467-018-05666-8)
6. Marchetti MC, Joanny JF, Ramaswamy S, Liverpool TB, Prost J, Rao M, Simha RA. 2013 Hydrodynamics of soft active matter. *Rev. Mod. Phys.* **85**, 1143–1189. (doi:10.1103/RevModPhys.85.1143)
7. Saw TB, Xi W, Ladoux B, Lim CT. 2018 Biological tissues as active nematic liquid crystals. *Adv. Mater.* **30**, 1802579. (doi:10.1002/adma.v30.47)
8. Mueller R, Yeomans JM, Doostmohammadi A. 2019 Emergence of active nematic behavior in monolayers of isotropic cells. *Phys. Rev. Lett.* **122**, 048004. (doi:10.1103/PhysRevLett.122.048004)
9. Kudrolli A, Lumay G, Volfson D, Tsimring LS. 2008 Swarming and swirling in self-propelled polar granular rods. *Phys. Rev. Lett.* **100**, 058001. (doi:10.1103/PhysRevLett.100.058001)
10. Simha RA, Ramaswamy S. 2002 Hydrodynamic fluctuations and instabilities in ordered suspensions of self-propelled particles. *Phys. Rev. Lett.* **89**, 058101. (doi:10.1103/PhysRevLett.89.058101)
11. Juelicher F, Kruse K, Prost J, Joanny JF. 2007 Active behavior of the cytoskeleton. *Phys. Rep.* **449**, 3–28. (doi:10.1016/j.physrep.2007.02.018)
12. Giomi L, Bowick MJ, Ma X, Marchetti MC. 2013 Defect annihilation and proliferation in active nematics. *Phys. Rev. Lett.* **110**, 228101. (doi:10.1103/PhysRevLett.110.228101)
13. Lemma LM, DeCamp SJ, You Z, Giomi L, Dogic Z. 2019 Statistical properties of autonomous flows in 2D active nematics. *Soft Matter* **15**, 3264–3272. (doi:10.1039/C8SM01877D)
14. Thampi SP, Golestanian R, Yeomans JM. 2014 Vorticity, defects and correlations in active turbulence. *Phil. Trans. R. Soc. A* **372**, 20130366. (doi:10.1098/rsta.2013.0366)
15. Doostmohammadi A, Shendruk TN, Thijssen K, Yeomans JM. 2017 Onset of meso-scale turbulence in active nematics. *Nat. Commun.* **8**, 1–7. (doi:10.1038/ncomms15326)
16. Pismen LM. 2013 Dynamics of defects in an active nematic layer. *Phys. Rev. E* **88**, 050502. (doi:10.1103/PhysRevE.88.050502)
17. Giomi L, Bowick MJ, Mishra P, Sknepnek R, Cristina Marchetti M. 2014 Defect dynamics in active nematics. *Phil. Trans. R. Soc. A* **372**, 20130365. (doi:10.1098/rsta.2013.0365)
18. Kawaguchi K, Kageyama R, Sano M. 2017 Topological defects control collective dynamics in neural progenitor cell cultures. *Nature* **545**, 327–331. (doi:10.1038/nature22321)
19. Saw TB *et al.* 2017 Topological defects in epithelia govern cell death and extrusion. *Nature* **544**, 212–216. (doi:10.1038/nature21718)
20. Balasubramaniam L *et al.* 2020 Nature of active forces in tissues: how contractile cells can form extensile monolayers. *bioRxiv*.
21. Vafa F, Bowick MJ, Shraiman BI, Marchetti MC. 2021 Fluctuations can induce local nematic order and extensile stress in monolayers of motile cells. *Soft Matter* **17**, 3068–3073. (doi:10.1039/D0SM02027C)
22. Killeen A, Bertrand T, Lee CF. 2021 Polar fluctuations lead to extensile nematic behavior in confluent tissues. Preprint. (https://arxiv.org/abs/2107.03838)
23. Shankar S, Ramaswamy S, Marchetti MC, Bowick MJ. 2018 Defect unbinding in active nematics. *Phys. Rev. Lett.* **121**, 108002. (doi:10.1103/PhysRevLett.121.108002)
24. Angheluta L, Chen Z, Marchetti MC, Bowick MJ. 2021 The role of fluid flow in the dynamics of active nematic defects. *New J. Phys.* **23**, 033009. (doi:10.1088/1367-2630/abe8a8)
25. Pismen LM, Sagués F. 2017 Viscous dissipation and dynamics of defects in an active nematic interface? *Eur. Phys. J. E* **40**, 92. (doi:10.1140/epje/i2017-11582-8)
26. Shankar S, Marchetti MC. 2019 Hydrodynamics of active defects: from order to chaos to defect ordering. *Phys. Rev. X* **9**, 041047.

21

royalsocietypublishing.org/journal/rspa *Proc. R. Soc. A* **478**: 20210879

27. Thijssen K, Nejad MR, Yeomans JM. 2020 Role of friction in multidefect ordering. *Phys. Rev. Lett.* **125**, 218004. (doi:10.1103/PhysRevLett.125.218004)

28. Pismen LM *et al.* 1999 *Vortices in nonlinear fields: from liquid crystals to superfluids, from non-equilibrium patterns to cosmic strings*, **vol. 100**. Oxford, UK: Oxford University Press.

29. Maitra A, Srivastava P, Marchetti MC, Lintuvuori JS, Ramaswamy S, Lenz M. 2018 A nonequilibrium force can stabilize 2D active nematics. *Proc. Natl Acad. Sci. USA* **115**, 6934–6939. (doi:10.1073/pnas.1720607115)

30. Guillamat P, Ignés-Mullol J, Shankar S, Marchetti MC, Sagués F. 2016 Probing the shear viscosity of an active nematic film. *Phys. Rev. E* **94**, 060602. (doi:10.1103/PhysRevE.94.060602)

31. Martínez-Prat B, Alert R, Meng F, Ignés-Mullol J, Joanny JF, Casademunt J, Golestanian R, Sagués F. 2021 Scaling regimes of active turbulence with external dissipation. Preprint. (https://arxiv.org/abs/2101.11570)

32. Alnæs M *et al.* 2015 The FEniCS project version 1.5. *Arch. Numer. Softw.* **3**, 9–23.

33. Logg A, Mardal KA, Wells GN. 2012 *Automated solution of differential equations by the finite element method*. Berlin, Germany: Springer.

34. Vafa F, Bowick MJ, Marchetti MC, Shraiman BI. 2020 Multi-defect dynamics in active nematics. Preprint. (https://arxiv.org/abs/2007.02947)

35. Zhang YH, Deserno M, Tu ZC. 2020 Dynamics of active nematic defects on the surface of a sphere. *Phys. Rev. E* **102**, 012607. (doi:10.1103/PhysRevE.102.012607)

36. Kreyszig E. 2011 *Advanced engineering mathematics (International student version)*, 10th edn. Hoboken: John Wiley & Sons, Inc.